 CMES, vol.29, no.3, pp.137-149, 2008

# Modeling 3D Fruit Tissue Microstructure Using a Novel Ellipsoid Tessellation Algorithm

**H.K. Mebatsion[1,2], P. Verboven[1], P. T. Jancsók[1], Q.T. Ho[1]**
**B.E. Verlinden[3] and B.M. Nicolaï[1,3]**

**Abstract:** Transport processes of gas and moisture are among the most important physiological processes in plant tissue. Microscale transport models based on Navier-Stokes equations provide insight into such processes at the microscopic scale. Due to microscopic complexity, numerical solutions based on the finite element or finite volume methods are mandatory. Therefore, a 3D geometric model of the tissue is essential. In this article, a novel algorithm for geometric reconstruction of 2D slices of synchrotron tomographic images is presented. The boundaries of 2D cells on individual slices were digitized to establish a set of boundary coordinates and the slice index of individual cells. Then, ellipsoids that fit these sets of points were determined using the Least Squared Fitted Ellipsoids (LSFEs) algorithm. This algorithm is a modified version of Minimum Volume Circumscribing Ellipsoid (MVCE) algorithm that produces minimum volume ellipsoids that encloses all sets of points. Using LSFEs, the size of the MVCEs were optimized to fit the set of points in a least square sense. The 3D model tissue geometry was then generated from these sets of ellipsoids, which were truncated when neighbouring volumes overlapped. As a result, a virtual 3D microstructure consisting of truncated ellipsoids fills up the entire volume with the same number of cells as that of the tomographic images.

**Keyword:** Multi-scale modelling, gas transport, water transport, virtual tissue, microtomography

[1] BIOSYST-MeBioS, Katholieke Universiteit Leuven, W. De Croylaan 42, B-3001 Leuven, Belgium
[2] Corresponding author. Phone: +32 16320590; E-mail: Hibru.Mebatsion@biw.kuleuven.be; Fax: +32 16322955
[3] Flanders Center of Postharvest Technology, W. De Croylaan 42, B-3001 Leuven, Belgium

## 1 Introduction

Biological systems are the most complex systems known to man. These systems develop naturally in a predefined bottom up manner without a purposeful human intervention. Despite a great deal of momentum in cell biology and fruit science, computational modelling of biological systems is at its infancy. This is amongst others due to the complicated cellular structure of biological systems leading to a large range of relevant length scales. It is impossible, for instance, to generate a finite element mesh that accurately represents the microstructure and also allows the numerical solution of the macroscopic structural component within a reasonable amount of time using the current computational systems [Kouznetsova, Brekelmans and Baaijens, (2001)]. To overcome these drawbacks, a multi-scale modelling approach is required. Multiscale modelling has a unique capability to simulate and link physical events occurring at different spatial and temporal scales. Accordingly, the existing elements of materials modelling, from quantum first principles simulations to meso- and macro-scale modelling, are unified in a self-consistent scheme [Fitzgerald, Goldbeck-Wood, Kung, Petersen, Subramanian and Westcott, (2008); Ma, Lui, Lu and Komanduri,(2006)], where each level of modelling generates information to be fed into the next level. By using multi-scale modelling, one thus passes through several characteristic length and time scales in which different physical models of varying levels of theoretical sophistication are applied and linked. This procedure is known as homogenization. Several techniques have been pro-

posed for simulation bridging two or more scales and at each scales simulation procedures have been well established. Yet, the treatment of transition regions from one scale to the other or the handshake region is a challenge [Ma, Lui, Lu and Komanduri, (2006)]. To implement the homogenization procedure, microstructure modelling is one component of the study. The difficulty of multi-scale material modelling lies in the geometric characterization and representation of complex biological systems.

Classical methods of characterizing microstructure of biological tissue usually involve viewing an image from a sectioned surface where the area of interest is stained and studied with an optical or scanning electron microscope [Uchic, Groeber, Dimiduk and Simmons, (2006); Groeber, Uchic, Dimiduk, Bhandari and Ghosh, (2006a)]. However, parameters such as connectivity, size and true shape can not be inferred from 2D sections. The need for complete characterization of 3D microstructures has led to the development of methods that allow one to directly obtain 3D microstructural information. One of the methodologies that have been successfully used is serial sectioning [Hakenberg and Shiflet, (2007); Kral and Spanos, (1999)]. Serial sectioning involves the acquisition of several 2D sections through the thickness of the material and the 3D reconstruction of the microstructure based on 2D information [Chawla and Chawla, (2006)]. However, the ability to produce serial sections of required resolution and field of view and at the required rate is limited. The serial sectioning procedure being carried out manually is also difficult to quantify, and any chemical used for staining is difficult to control [Groeber, Haley, Uchic, Dimiduk and Gosh, (2006b)]. This can lead to enhanced or reduced contrast of individual sections with subsequent image processing difficulties. Moreover, serial sectioning is prone to errors related to maintaining a constant sectioning thickness [Groeber, Haley, Uchic, Dimiduk and Gosh, (2006b)]. Despite some efforts to automate the serial sectioning procedure to get consistent sections [Spowart, (2006)], it is unlikely that serial sectioning will ever compete with non-destructive techniques such a high resolution X-ray microtomography.

X-ray micro-tomography provides detailed 3D microstructure information at as low as submicron resolution without sample preparation and chemical fixation [Larson, Yang, Ice, Budal, Tischler, (2002); Mendoza, Verboven, Mebatsion, Kerckhofs, Wevers and Nicolaï, (2007); Cloetens, Mache, Schlenker, Mach, (2006); Verboven, Kerckhofs, Mebatsion, Ho, Temst, Wevers, Cloetens, and Nicolaï, (2008)]. Segmented 3D microstructure data can readily be imported in finite element codes for computational engineering materials. Voxel based 3D microstructural geometries were used in computational testing of materials determine optimum microstructures in composite science [Mishnaevsky, 2005] and to investigate fracture related mechanical properties [Lee, Gokhale and Sreeranganathan, (2006)]. Nevertheless, the voxel based modelling approach has limitations when generating finite element meshes of anisotropic materials (such as biological materials). A massive amount of voxels are necessary to form a coherent and adequately covered modelling volume. Without reducing material information and by saving voxel positions, one would easily end up exceeding the current average memory size of desktop PCs. Hence, representative and computationally efficient 3D geometrical representation of microstructures remains a challenge. This is actually the case for biological materials. Biomaterials have non-trivial anisotropy but not all problems are sensitive to micro-structural details [Brahme, Alvi, Saylor, Fridy and Rollett, (2006)] and geometric simplification could result acceptable results. Even for a modest resolution, there is, therefore, a need for a geometric model representation of 3D microstructural images.

Methods to generate a representative 3D polycrystalline geometry based on microstructural data have been developed [Brahme, Alvi, Saylor, Fridy and Rollett, (2006); Groeber, Uchic, Dimiduk, Bhandari, Ghosh, (2006a); Groeber, Haley, Uchic, Dimiduk, Gosh, (2006b)]. Brahme, Alvi, Saylor, Fridy and Rollett, (2006)] combined the optimal ellipsoid packing approach and

Voronoi tessellation algorithms to represent the polycrystalline grain structure. The optimal packing procedure is essentially a search for a combination of ellipsoids that have no or small overlaps and fill the sample volume. Ellipsoidal radii and centres were determined by Electron Back Scatter Diffraction (EBSD) maps. Ellipsoids with randomly chosen centres and radii were placed in a box (equal to the size of the sample) and overlapping ellipsoids were discarded. When the volume of the optimally packed ellipsoids equalled the volume of the grains, the search for center points contained in only one of the ellipsoids continued. Finally, 3D Voronoi tessellations were generated based on the unique center points.

In a separate study on nickel based supper alloy (IN100) by Groeber et al. (2006b), an advanced version of the optimal filling ellipsoid approach was employed. The optimal ellipsoid filling procedure was similar with that of Brahme, Alvi, Saylor, Fridy and Rollett, (2006) except that they allowed a 5% of overlap. This leads to a massive amount of finite elements. Moreover, such microstructure data can hardly be parameterized and it is difficult to evaluate the sensitivity of the numerical solution to microstructural features.

Though optimal ellipsoid filling methods yielded virtual tissue geometries, it is apparent that such a geometric modelling approach results in geometries which are spatially different from the real microstructures. As shown in the study of metal deformation, geometrical models which are not a good representation of tissues may give simulated predictions completely different from experimental results [Chawla and Chawla, (2006)].

Mebatsion, Verboven, Ho, Mendoza, Verlinden, Nguyen and Nicolaï, (2006a) developed an ellipse tessellation algorithm to generate 2D geometric models of plant tissue microstructures that are spatially and statistically equivalent with microscopic images. The geometrical models were successfully interfaced with commercially available finite element codes (COMSOL Multiphysics, Stockholm, Sweden) for finite element simulation of gas and moisture transport [Mebatsion, Verboven, Ho, Mendoza, Verlinden, Nguyen and Nicolaï, (2006a)]. Yet, there are many microstructural features that can only be measured in 3D. These include the number of cell per unit volume, the true size and shape of microstructures and the connectivity of micro-structural features [Uchic, Groeber, Dimiduk and Simmons, (2006)]. Hence, there is a need for 3D characterization and quantification of microstructures.

This paper presents a 3D image based ellipsoid tessellation algorithm. This is an extension of the ellipse tessellation algorithm developed by Mebatsion, Verboven, Ho, Mendoza, Verlinden, Nguyen and Nicolaï, (2006a) to model 2D fruit microstructures. We will apply the algorithm to generate 3D virtual plant tissue microstructure based on synchrotron X-ray microtomography data. Pear fruit tissue will serve as a model system.

## 2 Materials and methods

### *2.1 Sample preparation*

Pears (*Pyrus communis* L. cv. 'Conference') were harvested on September, $13^{th}$ (optimal picking date) and $23^{rd}$ (late picking date), 2006, at the Fruitteeltcentrum (Rillaar, Belgium), cooled and stored according to commercial protocols for a period of 21 days at -0.5˚C, followed by CA storage (2.5 kPa $O_2$, 0.7 kPa $CO_2$ at -0.5˚C) until they were used for the experiments. Cylindrical samples of 5 mm diameter were taken from the fleshy part (parenchyma) of the pear tissue (Fig. 1).

### *2.2 X-ray microtomography*

X-rays are short wave radiations, which can penetrate through plant tissue. The level of transmission of these rays depends mainly on the mass density and mass absorption coefficient of the material [Salvo, Cloetens, Maire, Zabler, Blandin, Buffière, Ludwig, Boller, Bellet and Josserond, (2003)] allowing a distinction to be made between cellular material and air-filled pore spaces [Verboven, Kerckhofs, Mebatsion, Ho, Temst, Wevers, Cloetens and Nicolaï, (2008)]. The samples were enclosed in a glass tube to avoid dehydration. Microtomographic images were acquired at the European Synchrotron Radiation Facility (ESRF), Grenoble, France. The synchrotron radi-

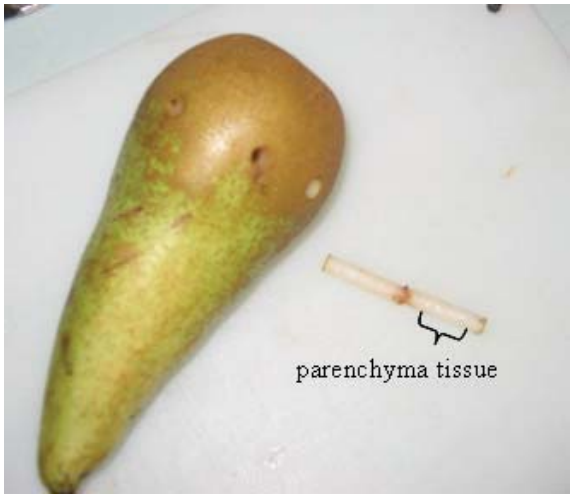


Figure 1: Conference pear and cylindrical parenchyma sample produced using a hollow cylindrical glass tube

ation tomography basically consists of recording a series of radiographs for different angular positions of the sample, which rotates around an axis perpendicular to the beam [Baruchel, Buffiere, Cloetens, Michiel, Ferrie, Ludwig, Maire and Salvo, (2006)]. When an X-ray beam is radiated towards a specimen, the incident ray may completely penetrate the specimen and recorded on a detector (CCD based detector for radiography). The filtered back-projection algorithm can then be used to reconstruct the volume of the sample from these radiographs. More details can be found in [Verboven, Kerckhofs, Mebatsion, Ho, Temst, Wevers, Cloetens and Nicolaï, (2008)].

### 2.3 *Digitization of microstructures*

In the tomographic images of 700 nm/pixel resolutions, the contrast between the pore space, the cell walls and the cells was too small for straightforward segmentation and edge detection. This calls for an extra image processing procedure known as digitization. Digitization of the cell boundaries is actually an approximation procedure, because the objects are constituted of pixels which have a discrete structure. In effect, the digital cell images were represented by a set of points defining the boundaries of every cell in a slice and the slice index, defining the third (z-) dimension. Only cells were digitized leaving intercellular spaces to be determined by the difference of the representative volume element (RVE) and cell volume. Fig. 2 shows the digitization and ellipsoid generation procedures.

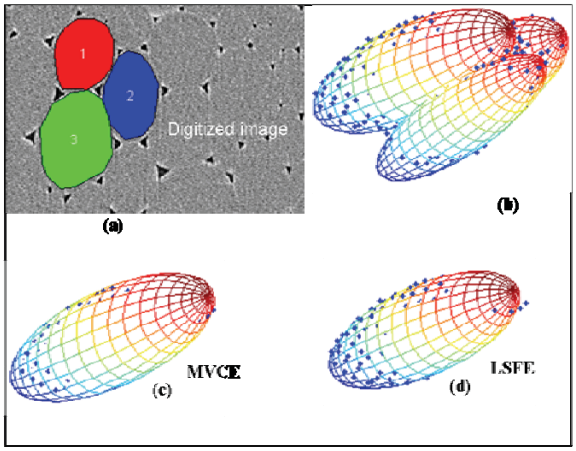


Figure 2: The digitization of tomographic images (a), the corresponding Least Squared Fitted Ellipsoids (LSFEs) (b), Minimum Volume Circumscribing Ellipsoid (MVCE) of the lower digitized cell (c) and the corresponding LSFE (d). The MVCEs and LSFE were constructed from digitized geometrical coordinates of the real tomographic images. The MVCE (c) of the lower digitized cell (cell 3) has larger radii ([32, 40,104$\mu$m]) than that of LSFE (d) ([31, 35, 97$\mu$m]).

### 2.4 *Three-dimensional visualization and modelling of fruit microstructure*

Studies on 2D microscopic images proved that the shape of pear fruit cells is approximately (truncated) elliptical [Mebatsion, Verboven, Ho, Mendoza, Verlinden, Nguyen and Nicolaï, (2006a); Mebatsion Verboven, Verlinden, Ho, Nguyen, Nicolaï (2006b)]. Mebatsion, Verboven, Ho, Mendoza, Verlinden, Nguyen and Nicolaï, (2006a) used ellipses to quantify the shape, aspect ratio and orientation of individual cells using a least square ellipse fitting algorithms. They modelled the fruit microstructure using ellipse tessellation algorithm in which cellular geometries which were represented by their equiv-

alent ellipses truncated when they overlapped. By doing so, statistically and spatially equivalent model geometries were generated, exported to finite element codes via interfacing Matlab (The Mathworks, Natick, MA) codes and used to perform computational (*in silico)* experimentation. Recent study by Verboven, Kerckhofs, Mebatsion, Ho, Temst, Wevers, Cloetens and Nicolaï, (2008) on 3D pear and apple microstructure also revealed that the shape of the cells is (truncated) ellipsoidal. Hence, we come up with algorithms to model fruit microstructure using ellipsoids characterized by microstructural information.

### 2.4.1 Minimum Volume Circumscribing Ellipsoid (MVCE)

The minimum volume circumscribing ellipsoid (MVCE) play an important role in several diverse applications such as optimal design [Titterington, (1978)], robust statistics and data mining in order to find the outliers in a given set of data (outliers can quickly be identified as points on the boundary of minimum volume covering ellipsoids) [Sun and Freund, (2004)].

The basic procedure goes as follows: Given a set $S$ of $m$ points in 3D, $S = \{p_1, p_2, p_3, \ldots, p_m\} \subseteq R^3$, there exists a unique ellipsoid that encloses the set of points that has a minimum volume. Denoting the minimum volume ellipsoid of the set $S$ by MVCE ($S$), and assuming the affine hull of the set $S$ spans $\mathrm{R}^3$, we can guarantee the circumscribing ellipsoid to have a positive volume. The general equation of an ellipsoid in a center form can be written as:

$$\varepsilon = \left\{ p_i \in \mathrm{R}^3 | (p_i - c) E (p_i - c)^T \leq 1 \right\} \tag{1}$$

where $c$ is the center of the ellipsoid $\varepsilon$ and **E** is a 3×3 the symmetric matrix. The matrix **E** determines the size and shape of the ellipsoid that encloses the set of points. The volume of the ellipsoid is given by

$$Vol(\varepsilon) = \frac{1}{\sqrt{\det(E)}} = \det(E^{-\frac{1}{2}}) \tag{2}$$

The problem of determining the MVCE containing the points S is thus equivalent to finding a vector $c \in \mathrm{R}^3$ and 3×3 positive definite symmetric matrix **E** which minimizes $\det(E^{-1})$ [Sun and Freund, (2004); Kumar and Yildirem, (2005); Saldanha, Coulomb, and Sabonnadiere, (1992); Gotoh and Konno, (2006)]. The overall optimization problem can be summarized as follows:

$$\begin{aligned} &\min_{E,c} \det(E^{-\frac{1}{2}}) \\ \text{subject to} \quad &(p_i - c) E (p_i - c)^T \leq 1 \\ &E > 0 \end{aligned} \tag{3}$$

When the number of points is large, solving the optimization problem of equation (3) can be expensive (the computation cost is proportional to the size of the set of points). However, the cost of solving the equation can drastically be reduced by defining polytopes determined by points that lie at the boundary of the set of points without compromising the accuracy of the solution [Gotoh and Konno, (2006)]. The polytopes that enclose the set of points were determined by defining a convex hull of the set of points (http://www.qhull.org).

Equation (3) is not a convex optimization problem unless the symmetric matrix, **E,** is a fixed positive definite matrix and the solution of such a problem is complicated [Fletcher, (1993)]. Thus, the optimization problem of equation (3) is modified and converted to a dual concave optimization problem that is easier to solve. In dual transformation, convex optimization problems are converted to concave optimization problems with the constraint equation becoming an optimised variable and vis-versa [Fletcher, (1993); Boyd and Vandenberghe, (2004)].

To guarantee that any ellipsoid containing a set of points has a positive volume and avoids trivial solutions individual points are lifted to 4D space by appending 1 as the 4th component of each of the points, $S' \subseteq \mathrm{R}^4$ [Sun and Freund, (2004)]. Then, the MVCE($S$) is determined by the intersection of the MVCE($S$') centred at the origin and the hyper plane $H = \left[\begin{smallmatrix} P \\ 1 \end{smallmatrix}\right]$ is a 4×n matrix [Kumar and Yildrem, (2005)]. This procedure gives rise to the modified convex optimization problem to com-

pute MVCE (S):

$$\begin{aligned} &\min_{M} \det(M^{-\frac{1}{2}}) \\ &\text{subject to} \quad \begin{bmatrix} p_i \\ 1 \end{bmatrix} M \begin{bmatrix} p_i^T & 1 \end{bmatrix} \leq 1 \\ &\qquad M > 0 \end{aligned} \tag{4}$$

where $M$ is a $4\times4$ symmetric and positive definite decision variable.

The Lagrangian dual form of equation (4) is equivalent to

$$\begin{aligned} &\min_{u} \; det(V(u)) = det \sum_{i=1}^{n} u_i \begin{bmatrix} p_i \\ 1 \end{bmatrix} \begin{bmatrix} p_i^T & 1 \end{bmatrix} \\ &\text{subject to} \quad e^T u = 1 \\ &\qquad u \geq 0 \end{aligned} \tag{5}$$

Where $u = [u_1, u_2, u_3, \ldots, u_n]$ is the decision variable and $e \in \mathrm{R}^n$denotes the vector of all ones.

After rearrangement and simplification we solve for the center of the ellipsoid and its $3\times3$ symmetric matrix as given in equation 7. For details refer to Kumar and Yildrem, (2005).

$$\begin{aligned} \mathrm{MVCE}(S) &= \varepsilon_{E,c} \\ &= \left\{ p_i \in \mathrm{R}^3 | (p_i - c) E (p_i - c)^T \leq 1 \right\} \end{aligned} \tag{6}$$

where

$$\begin{aligned} E &= (\frac{1}{3})(PUP^T - Pu^*(Pu^*)^T)^{-1} \\ c &= Pu^* \end{aligned} \tag{7}$$

and $\mathbf{U} = \mathrm{diag}(\mathbf{u}^*)$ is a diagonal matrix whose entries are given by components of $\mathbf{u}^*$, with $\mathbf{u}^*$ the solution of the optimization problem.

The symmetric matrix, **E**, and the center of ellipsoids, **c**, in equation (7) are determined by iterative calculation of $\mathbf{u}^*$ using Khachiyan's first order sequential linear programming algorithm for non-linear optimization problem [Todd and Yildrem, (2007)].

The algorithm was implemented in Matlab (The Mathworks, Natick, MA) to determine the MVCEs of the set of points on the boundaries of individual cells at every 10th slice of the microstructure. The cell digitization at every 10th slice, with slice interdistances of $0.7\mu$m, reduced the computation time and energy significantly without notable difference in the final ellipsoid tessellation result.

### 2.4.2 The Least squared Fitted Ellipsoid (LSFE)

The MVCEs is an enclosing algorithm that includes all set of points that define geometry. It is sensitive to minor digitization errors and as a result most of the time yields ellipsoids that are larger than the cells. To overcome this drawback, we forwarded a LSFE algorithm. The optimization involves a two step procedure. First, a MVCE of the set of points is determined. MVCE defines the size (radii) and the orientation of the ellipsoids. Using the radii as the initial guess, and keeping the orientation of the MVCEs, the LSFEs were optimized in such away that the sum of squared distances between the set of points and projected points on the surface of the ellipsoid is the minimum. The projected points on the ellipsoid lie on projected line connecting the centroid of the set of points and the set of points themselves. The procedure of determining a projected point on the surface of the ellipsoid is presented as follows. Let the MVCE algorithm produce an ellipsoid for the set of points shown in Fig. 3.

Suppose $q$ is a point a point on the MVCE obtained by the intersection of a projected line **L** through the centroid $x_0$of the MVCE and some data point $p$ and the MVCE.

A line, **L**, through the centroid of the set of points, $x_0$ meets the MVCE surface twice. Consider **L** and the MVCE, they intersected at $p$and $h$. Using line equation in a parametric form one can write:

$$q = x_0 + \alpha(p - x_0) \tag{8}$$

where $\alpha$ is a scalar defining the slope of **L**.

Moreover $q$ is also on the ellipsoid and the following equation holds:

$$(q-c)^T E (q-c) = 1, \tag{9}$$

where $c$ and $E$ are the center and $3\times3$ symmetric matrix of the MVCE, respectively.

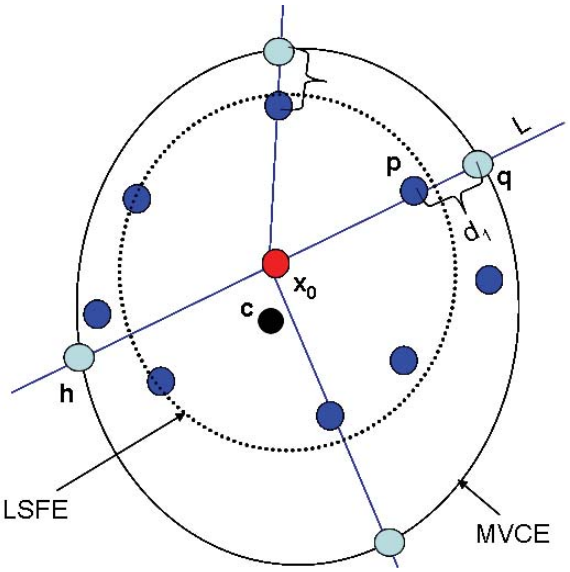


Figure 3: Least squares fitted ellipsoid (LSFE) determination procedure. The dotted line represents the boundary of LSFE whereas the solid is that of MVCE.

Substituting the line equation (8) in to the ellipsoid equation (9) and rearranging, we can get:

$$(\alpha(p-x_0)+(x_0-c))^T E(\alpha(p-x_0)+(x_0-c)) = 1 \quad (10)$$

Equation (10) is a quadratic equation of variable $\alpha$, which can be solved readily for$\alpha$. Subsequently, substitution of $\alpha$ in equation (8) yields $q$.

Finally, the LSFE is determined by searching for the ellipsoid that minimizes the sum of square distances of points and the corresponding projected points on the ellipsoid. The optimization was carried out using an in-house Matlab (The Mathworks, Natick, MA) based program. The comparison between MVCE and LSFE is presented in Fig. 2. In MVCE all points are enclosed inside the ellipsoid whereas in LSFE points lie in space in such a way that the sum of distance squares is minimized.

#### *2.4.3 Ellipsoid tessellation*

In 3D, the digital information of each cell in every $10^{th}$ slice, with slice interdistances of $0.7\mu$m of the tomographic image was gathered. Based on 2D cellular boundary coordinates of the tomographic slices and the slice index (representing the third dimension) the cells were approximated by ellipsoids using the LSFE algorithm. Once LSFEs of individual cells were determined, the model tissue geometry was generated from the ellipsoids, which were truncated when neighbouring volumes overlapped. As a result, as many truncated ellipsoids as there are cellular images were generated filling the entire 3D cellular volume.

The ellipsoid tessellation algorithm was implemented in Matlab 7.1 (The Mathworks, Natick, MA) programming environment.

Using the ellipsoid tessellation algorithms outlined above, 3D non-overlapping ellipsoidal regions that represent the fruit microstructure were generated. Fig. 4 shows three virtual cells, equivalent to digitized cells in Fig. 2, generated using the ellipsoid tessellation algorithm. The tessellation can be extended to as many representative volume elements (RVEs) as in the entire fruit microstructure in an effort to model the entire macroscale. As the ellipsoid tessellation algorithm is an image based microstructural generation procedure, it gives detailed information about the true nature of the structure. The statistical and spatial information of the microstructure that critically influence the numerical simulations of transport phenomena and mechanical deformation in biological or engineering material can be determined from the tessellation.

### *2.5 Calculations of the geometrical properties*

The geometrical parameters that characterize individual cells in 3D such as volume, and orientations of individual cells can be calculated from moment calculations. The three Euler angles that define the orientation of the cells from the three coordinate axes can be calculated readily from the orientation matrices. The ellipsoid tessellation algorithm gives a generalized $3\times3$ rotation matrix with elements:

$$R = \begin{bmatrix} r_{11} & r_{12} & r_{13} \\ r_{21} & r_{22} & r_{23} \\ r_{31} & r_{32} & r_{33} \end{bmatrix} \quad (11)$$

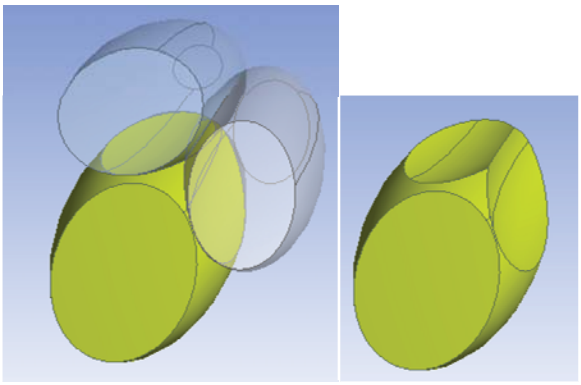

Figure 4: Ellipsoid tessellation algorithm applied to 3 neighbouring cells (left) and individual tessellated cell (right). Truncated surfaces are either the boundaries of the neighbouring cells or the intersection with the plane that defines the boundary of the RVE.

Where $R$ is calculated from the singular value decomposition of $\mathbf{E}$. $E = R\xi V$, with $R$ and $V$ are orthogonal $3\times3$ matrices and $\xi$ is a diagonal matrix.

This matrix can be considered as a sequence of three rotations, one about each principal axis, first about the $x$-axis, then $y$-axis and finally the $z$-axis, which can be represented as a matrix product (for details refer to Shoemake, 1985). The three Euler angles, $\psi$, $\phi$ and $\theta$ that define the orientation of individual cells are determined.

$$\theta = -\sin^{-}(r_{31}),\ \psi = \tan^{-}\left(\frac{r_{32}}{r_{33}}\right),\ \phi = \tan^{-}\left(\frac{r_{21}}{r_{11}}\right) \tag{12}$$

The volume of individual ellipsoid tessellation cells are calculated using convex hull functions (http://www.qhull.org/) implemented in Matlab (The Mathworks, Natick, MA). The porosity of the virtual microstructure was determined from the ratio of the volume of the pore space (Vs-Vc) (Vc is the volume of tessellated cells) and the volume of the sample (Vs).

### *2.6 Exporting geometries to finite element software package*

Individual ellipsoids that were determined by LSFE algorithm were exported in to ANSYS (ANSYS, Inc., Canonsburg, PA) via interfacing Matlab (The Mathworks, Natick, MA) code that converts surface geometries in to solid IGES (Initial Graphic Exchange Specification) file formats. IGES is a file format of data exchange in computer aided design (CAD) applications. The IGES file format is used by many programs as a standard ASCII text-based format for saving and exporting vector data; can store wireframe models, surface or solid object representations. The individual solid ellipsoids were as separate bodies and ellipsoids cut each other when they overlapped.

## 3 Results and discussions

3D ellipsoid tessellation virtual microstructures of pear dermal and parenchyma tissues are represented as shown in Fig. 5. These are the first geometrical representations of the 3D cell aggregates of fruit microstructure. The pore network can readily be determined from the difference of the total volume of the RVE and that of the 3D cell aggregates. Such geometrical representations reveal the complexity of the microstructure, its connectivity, coordination number and orientations of individual cells. There is a significant variation in the size and shape distributions of dermal and parenchyma cells. There is large variability in the size of the parenchyma cells than that of the dermal tissue. Dermal cells are more compact leaving smaller pore volume.

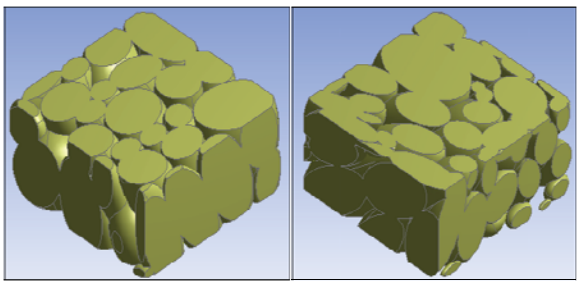

Figure 5: Ellipsoid tessellation geometry of pear dermal (left) and parenchyma (right) tissues in ANSYS (ANSYS, Inc., Canonsburg, PA) environment. Sample size is $179.2\times179.2\times84\ \mu$m.

The 3D pore network of the synchrotron images and its equivalent ellipsoid tessellation based pore

network are represented in Fig. 6. Surface approximation of discrete digital information has brought some variation in the continuity of the pore network (Fig. 6 (right)). This can be explained by changes in the size or shape of the cell geometry due to digitization, LSFE and tessellation algorithms. The isosurface reconstruction of tomographic images might have contributed as well. Yet, as a geometric model, the ellipsoid tessellation based pore network is a good representation of the microstructure.

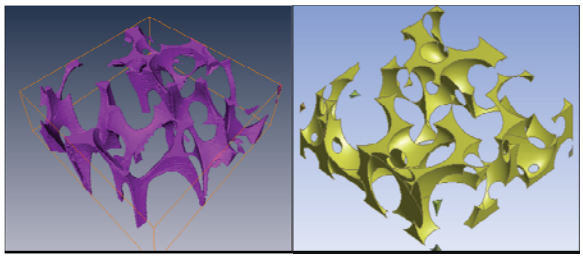

Figure 6: The pore network of the synchrotron image and its equivalent pore network of ellipsoid tessellation model ($315\times315\times84\mu$m).

The volume of the individual cells and the porosity of the microstructure can be calculated using the same software program used for ellipsoid tessellation. Fig. 7 shows the volume distribution of the pear dermal and parenchyma fruit microstructure based on six samples. The parenchyma cells are more variable than the dermal tissues, which is expressed by the standard deviation of cells volumes. The mean volumes of the dermal and parenchyma cells were calculated to be 1.32 $\pm1.42\times10^5$ $\mu$m$^3$ and 2.32 $\pm3.08\times10^5\mu$m$^3$, respectively. The porosity of the microstructures were calculated to be 9 $\pm$0.5 % and 10.3 $\pm$1.7% for dermal and parenchyma tissues, respectively. This value is in agreement with previous results that indicate samples comprising of epidermis and outer cortex tissues have smaller diffusivities than parenchyma tissue (Verboven, Kerckhofs, Mebatsion, Ho, Temst, Wevers, Cloetens, Nicolaï 2008). The calculated porosity value of pear parenchyma is larger than the experimental values of pear microstructure which about 5.1$\pm$1.5 (Mendoza, Verboven, Mebatsion, Kerckhofs, Wevers, Nicolaï 2007; Ho, Verlinden, Verboven, Nicolaï 2006). The difference might have been caused by the underestimation of the porosity value by the previous authors due to the inefficiency of the segmentation procedures or the overestimation of porosity by our tessellation algorithms. The biological variability, sample size and the length scale of the RVE could have contributed for the variation as well.

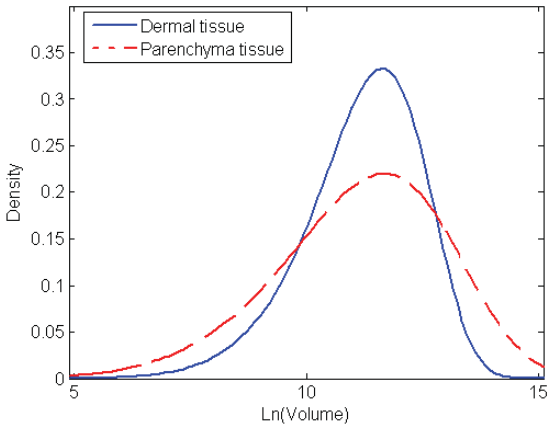


Figure 7: The volume distribution of pear dermal and parenchyma tissue. Volumes are in cubic $\mu$m. A Weibull distribution was fitted for the two data sets for ease of comparison. The figure is merely based on 6 samples per tissue.

Because fruit is a naturally occurring material, its microstructure is topologically disordered. This topological variation can be described by the neighbourhood of a cell with the others. The term coordination number is used to define the number of first neighbours. The coordination number is usually defined for pore networks as the number of pores in direct contact with a given pore. Nevertheless, the concept of coordination number can be extended to cells to quantify the relationship of cells in direct contact with a given cell. The average coordination number of cells of dermal and parenchyma tissues represented were calculated to be 5.25 $\pm$ 2.11 and 4.38 $\pm$ 2.18, respectively. The coordination number of the cells is related to the diffusion mass transport in fruit tissue and mechanical properties of the material, as the area and path of gas transport is inversely proportional to the number of neighbour cells. In other words, the concept of the cell coordination number is related

to the porosity of the material. Fruit tissue that has larger coordination number is likely to have shorter pore network paths and hence, has overall higher resistance to mass transport and smaller fractional air volume. Fruit with greater fractional air volumes have been shown to be softer [Yearsley, Banks, Ganesh, (1997a); Yearsley, Banks and Ganesh, (1997b); Volz, Harker, Hallet and Lang, (2004)] and to have greater internal gas diffusion rates [Rajapakse, Banks, Hewett and Cleland, (1990); Ho, Verlinden, Verboven and Nicolaï, (2006)]. The coordination number distribution of the dermal and parenchyma tissue is represented in Fig. 8. As can be seen from the figures the coordination number of the majority cells is between 2 to 8. The dermal tissue has greater coordination number than the parenchyma tissue, which is also expressed in terms of their porosity values but with a better perception of the geometry of the microstructure. The porosity of the fruit tissue might not give a clear picture as to the behaviour of transport phenomena. The interconnection of pores of the tissue is a very crucial component of multiscale modelling. Using the ellipsoid tessellation, we can visualize how pores are interconnected and conceptualize the transport phenomena through and, in the end, relate the geometries with the physiological disorders we are interested in. Fig. 10 shows the interconnectivity of pore structure in dermal and parenchymatic tissues of pear tissue. As can be seen from the figure, it is not only that the porosity of the material but also the connectivity of the pore structure that varies from tissue to tissue.

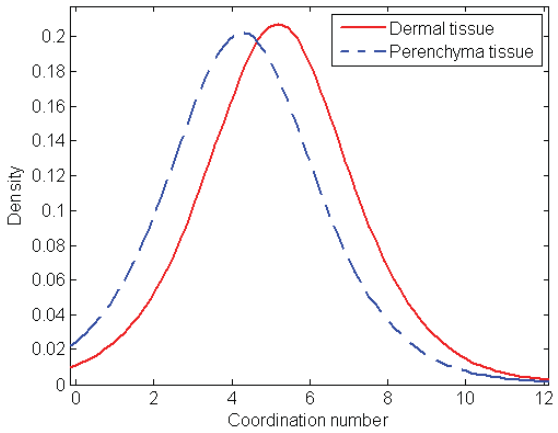


Figure 8: Coordination number distributions of dermal tissue and parenchyma tissue. Logistic distributions were fitted for the two coordination number data sets for ease of comparison.

## 4 Applications

Ellipsoid tessellation geometries will be used in the finite element simulation of gas and moisture transport and in the study of mechanical deformation of materials once interfaced with appropriate finite element or finite volume codes. In our research area, geometries will extensively be used in the multiscale modelling framework of fruit tissue. Simulations will be carried out at the lowest level by defining such detailed virtual microstructures and information are passed up the scale in order to understand the detailed mechanisms of physiological disorders in long term storage in cool rooms and mechanical deformations during postharvest handling.

The simulation of transport phenomena (gasses and water) at the microstructural level widens our knowledge about fruit-environment interactions and the evolution of physiological disorders core break down and internal browning in pear tissue. These disorders are characterized by textual changes, brown discoloration of tissue and development of cavities, which are not detectable from the outside. Though non-destructive methods such as magnetic resonance imaging (MRI) and X-ray computed tomography gave a good insight on the time course and spatial distribution of core breakdown, the mechanism of occurrence of these biological disorders and the continuous time course of the physiological changes is not known. In this respect, resolving the microstructure helps us understand physiological disorders induced by elevated $CO_2$ and decreased $O_2$ level in pear tissue during long-term storage better. In effect, this leads to a better cool room designs and efficient cool room operations.

On the other hand such a geometric representation of cells and intercellular spaces can helps us visualize microstructural details and increases our understanding about the nature of the fruit

microstructure. It gives us insight as to how transport phenomena in fruit tissue occur and the consequence of microstructural variability in the physiological response of fruits of different nature. Moreover, it helps us understand as to why different fruits have different transport and physicomechanical properties. Fig. 11 shows the detailed geometrical arrangement of some pear parenchyma cells in a pore networks in a given RVE tissue sample.

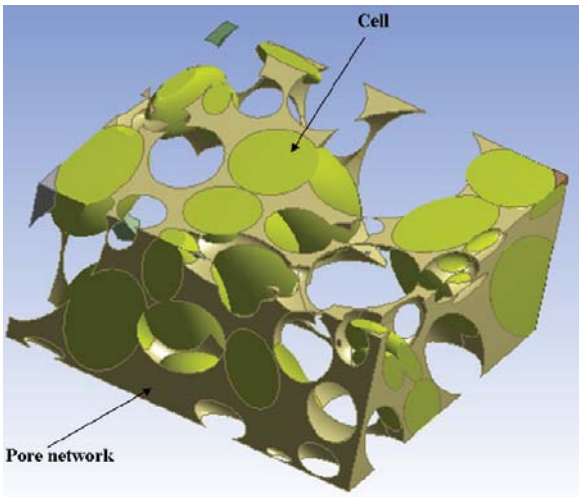


Figure 9: A geometric model of a pear parenchyma tissue showing the arrangement of some cells and interconnection of pores.

The geometrical models can be used in the simulation of gas and moisture transport in fruit tissues and in the investigation of mechanical deformation once the microstructural components such as cells, cell wall and pore network are precisely modelled, meshed, their material properties defined and appropriate boundary and initial conditions are defined. Fig. 10 shows the meshed geometry of the pear parenchyma tissue.

## 5 Conclusion

A novel 3D ellipsoid tessellation algorithm that generates representative fruit tissue geometry to be used in finite element/volume simulations was developed. Our algorithm excels previous attempts of material modelling by search of optimal ellipsoids that fills the desired volume by

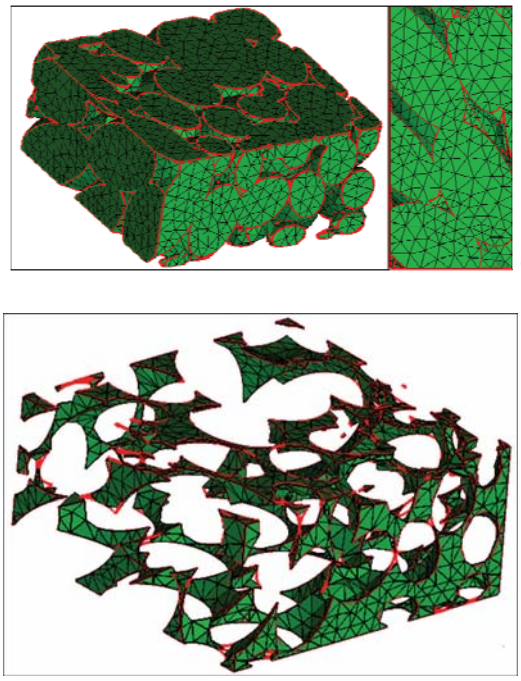


Figure 10: The geometric model of pear parenchyma tissue in finite volume environment (ICEM, CFD) a) cell interconnection; b) the pore network. Geometrical cell aggregate mesh (top left) and detailed mesh (top right).

Monte Carlo ellipsoid packing method. The algorithm produced image based virtual geometries that were exported to ANSYS (ANSYS, Inc., Canonsburg, PA) via an interfacing Matlab (The Mathworks, Natick, MA) codes. In effect, Matlab (The Mathworks, Natick, MA) surface geometries were converted in solid geometries which can be used for any CAD applications. The geometries will be used in multiscale modelling to perform computational (*in silico)* experimentation of gas and water transport in fruit tissues and mechanical deformation. This is one component of a series of efforts to understand the mechanism of physiological disorders (such as internal browning and core breakdown in pear tissues) in long term controlled atmosphere (CA) storage in cool rooms. The cell wall network geometric construction to include in the multiscale fruit tissue modelling is under separate study. This calls for accurate determination of the cell wall thickness using transmission electron microscopy (TEM).

**Acknowledgement:** Financial support by the Flanders Fund for Scientific Research (FWO-Vlaanderen) (project G.0200.02) and the K.U.Leuven (Research council scholarship for H.K. Mebatsion and IRO PhD scholarship for Q.T. Ho) are gratefully acknowledged. Pieter Verboven is Fellow of the Industrial Research Fund of the K.U.Leuven.

## References

**Baruchel, J.; Buffiere, J.Y.; Cloetens, P.; Michiel, M.D.; Ferrie, E.; Ludwig, W.; Maire, E.; Salvo, L.** (2006): Advances in synchrotron radiation microtomography. *Scripta Mater.* 55, pp 41-46.

**Boyd, S.; Vandenberghe, L.** (2004): *Convex optimization*. Cambridge University Press, UK.

**Brahme, A.; Alvi, M.H.; Saylor, D.; Fridy, J.; Rollett, A.D.** (2006): Three-dimensional reconstruction of microstructure in commercial purity aluminium. *Scripta Mater.* 55, pp 75-80.

**Chawla, N.; Chawla, K.K.** (2006): Microstructure based modelling of the deformation behaviour of particle reinforced metal matrix composites. *J. Mater. Sci.* 41, pp 913-925.

**Cloetens, P.; Mache, R.; Schlenker, M.; Mach, S.L.** (2006): Quantitative phase tomography of Arabodopsis seeds reveals intercellular void network. *PNAS* 103, pp 14626-14630.

**Fitzgerald, G.; Goldbeck-Wood, G.; Kung, P.; Petersen, M.; Subramanian, L.; Wescott, J.** (2008): Materials modeling from quantum mechanics to the mesoscale. *CMES: Computer Modeling in Engineering & Sciences* 24(3), pp 169-183.

**Fletcher, L.** (1993): *Practical methods of optimization.* John Wiley & Sons Ltd, Chichester, UK.

**Gotoh, J.; Kanno, H.** (2006): Minimal ellipsoid circumscribing a polytope defined by a system of linear inequalities. *J. Global Optim.* 34, pp 1-14.

**Groeber, M.; Uchic, M.D.; Dimiduk, D.M.; Bhandari, Y.; Ghosh, S.** (2006): *The third multiscale material modelling international conference: Conference proceeding*, pp 438-446, Frieburg, Germany.

**Groeber, M.A.; Haley, B.K.; Uchic, M.D.; Dimiduk, D.M.; Gosh, S.** (2006): Three-dimensional reconstruction and characterization of polycrystalline microstructures using a FIB-SEM system. *Mater. Charact.* 57, pp 259-273.

**Hakenberg, R.H.; Shiflet, G.J.** (2007): A serial sectioning technique for evaluating grain and twin boundary precipitate growth kinetics in bulk specimens. *Mater. Charact.* 58, pp 211-219.

**Ho, Q.T.; Verlinden, B.E.; Verboven, P.; Nicolaï, B.M.** (2006): Gas diffusion properties at different positions in the pear. *Postharvest Biol. Technol.* 41, pp 113-120.

**Kouznetsova, V.; Brekelmans, W.A.M.; Baaijens, F.P.T.** (2001): An approach to micro-macro modelling of heterogeneous materials. *Comput. Mech.* 27, pp 37-48.

**Kral, M.V.; Spanos, G.** (1999): Three-dimensional analysis of proeutectoid cementite precipitates. *Acta Materialia* 47, pp 711-724.

**Kumar, P.; Yildrem, E.A.** (2005): Minimum volume circumscribing ellipsoids (MVCE) s and core sets. *J. Optimiz. Theory App.* 126, pp 1-121.

**Larson, B.C.; Yang, W.; Ice, G.E.; Budal, J.B.; Tischler, J.Z.** (2002): Three-dimensional X-ray structure microscopy with sub-micrometer resolution. *Nature* 415, pp 887-890.

**Lee, S.G.; Gokhale, A.M.; Sreeranganathan, A.** (2006): Reconstruction and visualization of complex three-dimensional pore morphologies in a high-pressure die-cast magnesium alloy. *Mat. Sci. Eng. A-Struct.* 427, pp 92-98.

**Luo, Z.Q.; Yu, W.** (2006): An introduction to convex optimization for communications and signal processing. *IEEE journal on selected areas in communications* 24(8), pp 1426-1438.

**Ma, J.; Lui, Y.; Lu, H.; Komanduri, R.**(2006): Multiscale simulation of Nanoindentation using the generalized interpretation material point (GIMP) method, dislocation dynamics (DD) and molecular dynamics (MD). *CMES: Computer Modeling in Engineering & Sciences* 16(1), pp 41-55.

**Mebatsion, H.K.; Verboven, P.; Ho, Q.T.; Men-**

**doza, F.; Verlinden, B.; Nguyen, A.T.; Nicolaï, B.M.** (2006a): Modeling fruit microstructure using novel ellipse tessellation algorithm. *CMES: Computer Modeling in Engineering & Sciences* 14(1), pp 1-14.

**Mebatsion, H.K.; Verboven, P.; Verlinden, B.; Ho, Q.T.; Nguyen, A.T.; Nicolaï, B.M.** (2006b): Microscale modelling of fruit tissue using Voronoi tessellations. *Comput. Electron. Agric.* 52, pp 36-48.

**Mendoza, F.; Verboven, P.; Mebatsion, H.K.; Kerckhofs, G.; Wevers, M.; Nicolaï, B.M.** (2007): Three-dimensional pore space quantification of apple tissue using x-ray computed microtomography. *Planta* 226(3), pp 559-570.

**Mishnaevsky, Jr.L.L.** (2005): Automatic voxel based generation of three-dimensional microstructural FE models and its application to the damage analysis of composites. *Mat. Sci. Eng. A-Struct* 407, pp 11-23.

**Rajapakse, N.C.; Banks, N.H.; Hewett, E.W.; Cleland, D.J.** (1990): Development of oxygen concentration gradients in flesh tissues of bulky plant organs. *J. Amer. Soc. Hortic. Sci.* 115, pp 793-797.

**Saldanha, R.R.; Coulomb, J.L.; Sabonnadiere** (1992): An ellipsoid algorithm for the optimum design of magnetostatic problem. *IEEE transactions on magnetics* 28(2), pp 1573-1576.

**Salvo, L.; Cloetens, P.; Maire, E.; Zabler, S.; Blandin, J.J.; Buffière, J.Y.; Ludwig, W.; Boller, E.; Bellet, D.; Josserond, C.** (2003): X-ray microtomography an attractive characterization technique in materials science. *Nuc. Instrum. Meth. B*, 200, pp 273-286.

**Shoemake, K.** (1985): Animating rotation with quaternion curves. *Proc. SIG-GRAPH*, 19, pp 245-254.

**Spowart, J.E.** (2006): Automated serial sectioning for three-dimensional analysis of microstructures. *Scripta Mater.* 55, pp 5-10.

**Sun, P.; Freund, R.M.** (2004): Computation of minimum volume covering ellipsoids. *Operational research* 52(5), pp 690-706.

**Titterington, D.M.** (1978): Estimation of correlation coefficients by ellipsoid trimming. *Applied statistics* 27, pp 227-234.

**Todd, M. J.; Yıldırım, E. A.** (2007): On Khachiyan's algorithm for the computation of minimum-volume enclosing ellipsoids. *Discrete Appl. Math.* 155, pp 1731-1744.

**Uchic, M.D.; Groeber, M.A.; Dimiduk, D.M.; Simmons, J.P.** (2006): Three-dimensional microstructural characterization of nickel super alloys via serial-sectioning using a dual beam FIB-SEM. *Scripta Mater.* 55, pp 23-28.

**Verboven, P.; Kerckhofs, G.; Mebatsion, H.K.; Ho, Q.T.; Temst, K.; Wevers, M.; Cloetens, P.; Nicolaï, B.M.** (2008): 3-D gas exchange pathways in pome fruit characterised by synchrotron X-ray computed tomography. *Plant Physiol.* (accepted).

**Volz, R.K.; Harker, F.R.; Hallet, I.C.; Lang, A.** (2004): Development of texture in apple fruit – a biophysical perspective. *Acta Hort.* 636, pp 473-479.

**Yearsley, C.W.; Banks, N.H.; Ganesh, S.** (1997a): Temperature effects on the internal lower oxygen limits of apple fruit. *Postharvest Biol. Technol.* 11, pp 73-83.

**Yearsley, C.W.; Banks, N.H.; Ganesh, S.** (1997b): Effects of carbon dioxide on the internal lower oxygen limits of apple fruit. *Postharvest Biol. Technol.* 12, pp 1-13.